# Structural and magnetic interplay in multiferroic $Ho_{0.5}Nd_{0.5}Fe_3(BO_3)_4$

A. Tripathy,[1] K. Gautam,[1,*] K. Dey,[1] S. R. Sahu,[1] A. Ahad,[2,†] A. Upadhyay,[3] A. Sagdeo,[3,4] S. Francoual,[5] P. J. Bereciartua,[5] I. Gudim,[6] J. Strempfer,[5,‡] V. G. Sathe,[1] and D. K. Shukla[1,§]

[1]*UGC-DAE Consortium for Scientific Research, Indore 452001, India*

[2]*Department of Physics, Aligarh Muslim University, Aligarh 202002, India*

[3]*Accelerator Physics and Synchrotrons Utilization Division, Raja Ramana Centre for Advance Technology, Indore 452013, India*

[4]*Homi Bhabha National Institute, Training School Complex, Anushakti Nagar, Mumbai 400094, India*

[5]*Deutsches Elektronen-Synchrotron, Notkestrasse 85, D-22607 Hamburg, Germany*

[6]*L. V. Kirensky Institute of Physics, Siberian Branch of Russian Academy of Sciences, Krasnoyarsk 660036, Russia*

(Received 26 January 2023; accepted 22 May 2023; published 23 June 2023)

Rare-earth iron borates, $RFe_3(BO_3)_4$ ($R$ = rare earth), are of considerable interest because of their structural and magnetic complexities due to the involvement of both 3*d* and 4*f* magnetic interactions in a helical lattice. Among them $Ho_{0.5}Nd_{0.5}Fe_3(BO_3)_4$ has attracted the most attention, as it exhibits a multiferroic property with a large, spontaneous, and magnetic-field-induced electric polarization ($P$) below the antiferromagnetic transition temperature ($T_N \sim 32$ K). This compound has been reported to be noncentrosymmetric (nonpolar) down to the lowest temperature, and the origin of spontaneous electric polarization below $T_N$ is not known. By utilizing temperature-dependent synchrotron x-ray powder diffraction, we report here the observation of structural phase transition, i.e., the lowering of crystal symmetry from $R32$ to $P3_121$ below $T_N$ in $Ho_{0.5}Nd_{0.5}Fe_3(BO_3)_4$, which is further confirmed by single-crystal x-ray diffraction measurements as well as substantiated by dielectric and Raman spectroscopic results. With the help of x-ray resonant magnetic scattering, we have studied the element-specific magnetic ordering behavior, and by combining all the results, we show that the spontaneous electric polarization below the antiferromagnetic ordering transition emerges through the *p-d* hybridization mechanism associated with the $FeO_6$ octahedra. The observations of subtle structural changes at low temperature and element-specific magnetic ordering behavior provide a comprehensive understanding of the multiferroicity in this family of compounds.

DOI: 10.1103/PhysRevB.107.214106

## I. INTRODUCTION

Multiferroics, wherein magnetic and electric properties coexist, have attracted great attention during the last two decades. Besides the presence of multiple ordered states, these compounds are fascinating also because of the cross coupling between them, which provides an opportunity to manipulate the electric polarization (by magnetic field) and magnetization (by electric field), which has an essential role in device applications and manifests many interesting and rich fundamental physics problems [1–3]. Based on the microscopic origin, multiferroics are classified into type-I and type-II, where the type-II multiferroics exhibit ferroelectricity of magnetic origin, having strong magnetoelectric (ME) coupling. Spontaneous ferroelectric polarization in these compounds emerges due to spins with strong magnetic anisotropy, frustrated spin structure (noncollinear), charge ordering (orbital hybridization), and coupling of the spins with the lattice, which are the basis of breaking the inversion symmetry. The crystal symmetry in these materials is strongly influenced by magnetic ordering. Lattice distortion due to the magnetic ordering relieves frustration and ferroelectric polarization emerges. This phenomenon is very robust and is identified in the structural, dielectric, and ferroelectric properties [4–7].

$RFe_3(BO_3)_4$ compounds have received a lot of attention because of their complex magnetic structure, strong ME coupling, and nonlinear optical properties [8–20]. They crystallize in the noncentrosymmetric trigonal structure (huntite type) with space group either $R32$ or $P3_121$, which depends on the ionic radii of the rare earth [21,22]. Compounds with smaller ionic radii ($R$ = Eu-Er,Y) undergo a weak structural transition from high-symmetry phase $R32$ to a low-symmetry phase $P3_121$ [22]. These compounds are more interesting from the symmetry point of view, as most of them belong to the chiral point group ($D_3$) [23,24]. They possess structural peculiarities having edge-sharing $FeO_6$ octahedra that form a helicoidal chain parallel to the crystallographic $c$ axis, which is interconnected by $BO_3$ triangles and $RO_6$ trigonal prisms. The presence of distinct magnetic sublattices of $Fe^{3+}$(3*d*) and $R^{3+}$(4*f*) ions influence the magnetic properties and antiferromagnetic (AFM) transition temperature ($T_N \sim 30$–40 K,

*Present address: RIKEN Center for Emergent Matter Science, 2-1 Hirosawa, Saitama 351-0198, Japan.

†Present address: School of Physical and Mathematical Sciences, Nanyang Technological University, Singapore.

‡Present address: Advanced Photon Source, Argonne National Laboratory, Lemont, Illinois 60439, USA.

§Corresponding author: dkshukla@csr.res.in

 

depending upon the ionic radii of rare earth), and in some cases the AFM transition is followed by a spin reorientation transition $T_{SR}$ at lower temperature [9,10,25]. The AFM transition in $R$Fe$_3$(BO$_3$)$_4$ is mostly governed by the $Fe^{3+}$ ions through Fe-O-Fe superexchange interaction, as the direct R-O-R exchange pathways are absent. However, there is superexchange path between R and Fe through the R-O-Fe chains, causing *f-d* exchange interaction. These compounds form an important class of type-II multiferroics, and ME coupling has been discussed intensively through magnetostriction and magnetodielectric experiments [11,25,26].

Among the $R$Fe$_3$(BO$_3$)$_4$ compounds, HoFe$_3$(BO$_3$)$_4$ undergoes a structural transition at ∼366 K and an AFM transition at $T_N$ ∼ 38 K, which is followed by a spin reorientation transition at $T_{SR}$ ∼ 5 K [27–29]. Another important member of this family, NdFe$_3$(BO$_3$)$_4$, orders antiferromagnetically at $T_N$ ∼ 31 K but does not undergo structural transition (remains in $R32$) and does not exhibit spin reorientation transition down to the lowest temperature [30]. Surprisingly, a mix of the above two [in 50:50 ratio, i.e., Ho$_{0.5}$Nd$_{0.5}$Fe$_3$(BO$_3$)$_4$] exhibits an AFM transition shifted downwards to $T_N$ ∼ 32 K and a spin reorientation transition at a slightly higher temperature $T_{SR}$ ∼ 9 K as in HoFe$_3$(BO$_3$)$_4$. It is interesting to note that both the spontaneous as well as the field-induced polarizations are enhanced drastically in this compound compared to the parent compounds [10]. However, 75% Nd doping at the Ho site does not create any substantial change and the spontaneous polarization decreases [29]. The effect of easy-axis and easy-plane magnetic anisotropies and the ME coupling behavior in Ho$_{0.5}$Nd$_{0.5}$Fe$_3$(BO$_3$)$_4$ has been discussed earlier in the context of magnetodielectric and x-ray magnetic circular dichroism studies with the application of magnetic field [10,31,32]. However, these measurements cannot explain the driving mechanism of the appearance of spontaneous polarization without considering symmetry analysis. Moreover, it is also important to note that the parent compounds have different crystal symmetries and magnetic anisotropies of rare earths [in HoFe$_3$(BO$_3$)$_4$, Ho has easy-axis, and in NdFe$_3$(BO$_3$)$_4$, Nd has easy-plane anisotropy] [10,30,33]. Under magnetic field, Ho$_{0.5}$Nd$_{0.5}$Fe$_3$(BO$_3$)$_4$ carries properties of both parent compounds, as polarization along $P_a$ decreases (H ∥ $c$) as in HoFe$_3$(BO$_3$)$_4$ and increases almost twice (H ∥ $a$) as compared to NdFe$_3$(BO$_3$)$_4$ [10,17,34]. Polarization in the ordered magnetic phase with three different magnetic sublattices may accompany a possible lattice distortion that has not been experimentally verified in this compound. This points to the importance of a careful crystallographic structure determination of Ho$_{0.5}$Nd$_{0.5}$Fe$_3$(BO$_3$)$_4$. Earlier hard x-ray scattering studies on $R$Fe$_3$(BO$_3$)$_4$ ($R$= Tb and Gd) have shown the presence of forbidden structural superlattice reflections (0,0,1) and (0,0,2) in the magnetic ordered phase ($P3_121$), evidencing small structural distortion [12]. The emergence of spontaneous electric polarization in Ho$_{0.5}$Nd$_{0.5}$Fe$_3$(BO$_3$)$_4$ below the magnetic ordering is second sight that the lattice might be playing a very crucial role. Although the compound is noncentrosymmetric in the $R32$ phase (paramagnetic), no ferroelectricity should appear, as it is nonpolar. Therefore, because of the intrinsic structural intricacies in this compound, we have focused on the role of lattice degrees of freedom across the magnetic ordering.

Here we present temperature-dependent crystal structure studies of Ho$_{0.5}$Nd$_{0.5}$Fe$_3$(BO$_3$)$_4$ which is complimented by Raman, magnetization, and dielectric measurements. The magnetization measurement confirms the AFM transition at $T_N$ ∼ 32 K. The Raman and dielectric spectroscopic studies show the signatures of a structural change below the AFM transition. Synchrotron x-ray powder diffraction (SXPD) and single crystal x-ray diffraction (SCXD) studies confirm the structural transition at $T_N$, and the change of crystal symmetry from $R32$ to $P3_121$ is shown by Rietveld refinement. The x-ray resonant magnetic scattering (XRMS) study provides information about the temperature evolution of moments of all three magnetic sublattices (Fe, Ho, and Nd). Structural results show that the changes in the temperature evolution of Fe-O bond length is found directly associated with the $Fe^{3+}$ spins (Fe-O-Fe exchange interactions) and provides strong evidence for the appearance of polarization through *p-d* hybridization.

## II. EXPERIMENT

The Ho$_{0.5}$Nd$_{0.5}$Fe$_3$(BO$_3$)$_4$ single crystals were grown from the flux method with bismuth trimolybdate 82 wt % [Bi$_2$Mo$_3$O$_{12}$ + 3B$_2$O$_3$ + 0.25Ho$_2$O$_3$ + 0.25Nd$_2$O$_3$] + 18 wt % Ho$_{0.5}$Nd$_{0.5}$Fe$_3$(BO$_3$)$_4$ as described elsewhere in detail [32]. Single crystals of size around 4 × 3 × 1 mm were used in the experiments. Temperature-dependent dielectric measurements were performed on both parallel to $c$-axis and *ab*-plane oriented crystals. Measurements were performed inside a Quantum Design 14T PPMS using a homemade insert with a HIOKI(IM 3536) LCR meter. The data was taken in both heating and cooling cycles at a rate of 1 K/min. Pyrocurrent measurements were performed by utilizing a Keithley electrometer 6517B. The sample was first cooled down to the lowest temperature and left short-circuited for 30 min in order to remove any possible trapped stray or interfacial charge carriers. The data was collected while heating at a rate of 3 K/min. Raman spectroscopic studies were carried out in a backscattering configuration using a LabRam HR800 system equipped with a liquid helium cryogenic facility. An Ar+ laser of 473 nm as excitation source, 1800 g/mm grating, and a charge coupled device (CCD) detector was used for the measurements. Magnetization measurements were carried out following a zero-field-cooled (ZFC) protocol from 2 to 100 K under applied magnetic field of 1000 Oe using a Quantum Design 16T VSM. During the measurement the magnetic field was applied parallel to the *ab* plane. The SXPD data were collected on powdered single crystals mounted in a He flow cryostat at the BL-12 beamline of the Indus-II synchrotron source at RRCAT, Indore, India. The SXPD experiment was performed using high-energy photons ($\lambda$ = 0.81632 Å) and an area detector (MAR 345) of 100-$\mu$m$^2$ pixel size. Rietveld refinement has been utilized for the analysis of powder diffraction data with the FULLPROF SUITE, and the schematic of the crystal structure was drawn using VESTA [35,36]. Single-crystal resonant and nonresonant x-ray diffraction studies were performed at the P09 beamline at the PETRA III synchrotron at DESY, Hamburg, Germany [37]. XRMS experiments were performed across the $L$ edges of Ho and Nd and the $K$ edge of Fe atoms in both vertical as well and horizontal scattering geometries. The magnetic wave

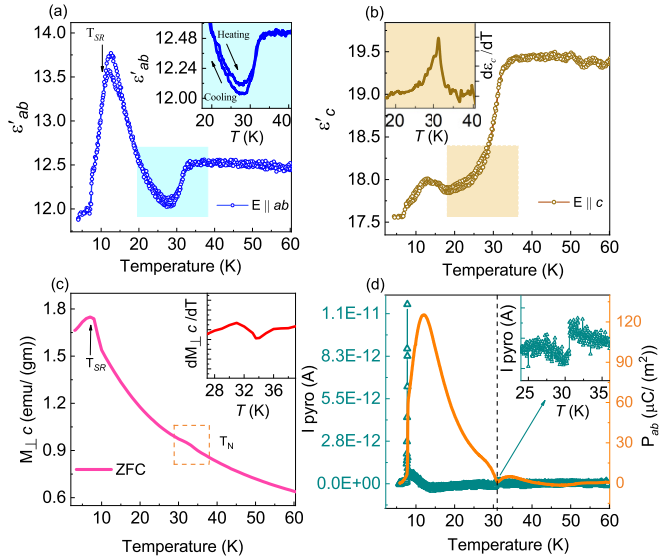


FIG. 1. Temperature-dependent dielectric permittivity at 100 kHz along the *ab* plane (a) and along the *c* axis (b) of $Ho_{0.5}Nd_{0.5}Fe_3(BO_3)_4$ single crystal. Inset of (a) and (b) shows the hysteresis of $\varepsilon'_{ab}$ and derivative of $\varepsilon'_c$ around $T_N$, respectively. (c) The magnetization vs temperature measured in ZFC protocol perpendicular to *c* axis under 1000 Oe magnetic field, and inset shows $dM_\perp c/dT$ vs T. (d) Pyrocurrent and polarization ($\boldsymbol{P}_{ab}$) at zero magnetic field and inset shows the zoomed view around $T_N$.

vector of the compound is (0,0,1.5) [8,33]. Vertical scattering experiments were performed at the P09 beamline using Psi diffractometer (EH1) and a closed cycle cryostat, whereas the horizontal scattering experiments were performed at the same beamline using the heavy load diffractometer (EH2). In both geometries the *ac* plane was oriented in the scattering plane. Copper (1,1,0) and PG (0,0,6) crystals were used as analyzers at the Nd/Fe edges and Ho edge, respectively. The temperature-dependent behavior of Bragg reflection (1,2,6) was measured at the same beamline using photons of 6.728 keV energy.

## III. RESULTS

### A. Electrical and magnetic properties

Temperature- and frequency-dependent dielectric measurements were performed along two axes (E ∥ *ab* and E ∥ *c*) of the $Ho_{0.5}Nd_{0.5}Fe_3(BO_3)_4$ single crystal. Steplike anomalies were observed in the real part of the permittivity around $T_N$ along both axes [see Figs. 1(a) and 1(b)]. A similar steplike behavior was reported in the dielectric data across the structural transitions in $GdFe_3(BO_3)_4$ and $TbFe_3(BO_3)_4$ [11,38]. To better understand the nature of the transition, we performed measurements in both heating and cooling cycles. Surprisingly, we observed a thermal hysteresis across the AFM transition temperature [see inset of Fig. 1(a)] which indicates the first-order nature of this transition. The dielectric permittivity measured along the *ab* plane matches well with the earlier reported *a*-axis data [32], and the *c*-axis data follows a similar temperature dependent behavior. The inset of Fig. 1(b) shows the derivative of the heating cycle data measured along the *c* axis, which marks the transition temperature slightly above ∼30 K. Features in the dielectric permittivity measurements in this compound are found to be frequency independent. The peaklike feature at ∼9 K along both axes corresponds to the spin reorientation ($T_{SR}$) transition. Spin reorientation is a first-order transition and arises due to the spin flop of the $Fe^{3+}$. It has been found by magnetization and specific heat measurements reported earlier [10,32].

Magnetization measurement shows a small hump at $T_N$ ∼ 32 K and a downturn at $T_{SR}$ [see Fig. 1(c)]. The inset shows a derivative of the magnetization curve at the AFM transition. Anomalies in the magnetization data match well with the reported data [32]. In order to monitor the spontaneous electric polarization, pyrocurrent measurement at zero magnetic field was performed, which shows a sharp change at $T_N$ as also observed in the dielectric data [inset of Fig. 1(d)]. Polarization ($\boldsymbol{P}_{ab}$) is obtained by integrating the current over time. We observe a slow increase in $\boldsymbol{P}_{ab}$ at $T_N$ with a rise at ∼25 K and a sudden drop at $T_{SR}$ [Fig. 1(d)]. Finally, the steplike anomaly in dielectric data shows an indication of a structural change, and the simultaneous emergence of spontaneous polarization clearly indicates the formation of electric dipole moments which is related to changes in the symmetry of this compound below the AFM transition.

### B. Raman spectroscopy

Raman spectroscopy is highly sensitive to structural (local) changes and is an invaluable tool for studies of phonons. It has been extremely useful for the studies of multiferroics, as changes of structural and magnetic orders coupled with crystal lattice manifest directly in the vibrational spectrum (spin-phonon coupling). To understand the behavior of phonons in $Ho_{0.5}Nd_{0.5}Fe_3(BO_3)_4$ across the AFM transition, we performed temperature-dependent unpolarized Raman spectroscopy on its single crystal, in the range 5–60 K. Earlier Raman experiments on $RFe_3(BO_3)_4$ ($R$ = Nd, Gd, Tb, Er) have determined the external and internal vibrational modes using the factor group analysis both in the high-symmetry $R32$ ($D_3^7$) and low-symmetry phase $P3_121$ ($D_3^4$) [39]. The $R32$ phase (one formula unit) exhibits 26 Raman active modes characterized as $\Gamma_{vib} = 7A_1 + 12A_2 + 19E$, while in the $P3_121$ phase (two formula units) there are 86 Raman active modes which are classified as $\Gamma_{vib} = 27A_1 + 32A_2 + 59E$. Here, the $A_1$ and E modes are Raman active and $A_2$ are acoustic modes. The phonon frequencies originating below 550 $cm^{-1}$ were considered as external modes which are mostly $A_1$ and E modes and internal modes are dominated by vibrations of $BO_3$ structural unit which appear at relatively higher frequencies, above 550 $cm^{-1}$. Within our experimental resolution, at the structural transition not all the modes are experimentally visible; however, noticeable changes were observed in the Raman vibrational frequency range of 200 $cm^{-1}$ to 600 $cm^{-1}$ [Fig. 2(a)]. We observe some unusual shifting as well as an appearance of new Raman modes close to $T_N$ ∼ 32 K and becoming more prominent below ∼25 K.

The most prominent changes we have observed are in the external modes, mostly at ∼318 $cm^{-1}$, ∼337 $cm^{-1}$, ∼372 $cm^{-1}$, ∼402 $cm^{-1}$, and ∼479 $cm^{-1}$. By comparing the experimental results with the previously simulated factor

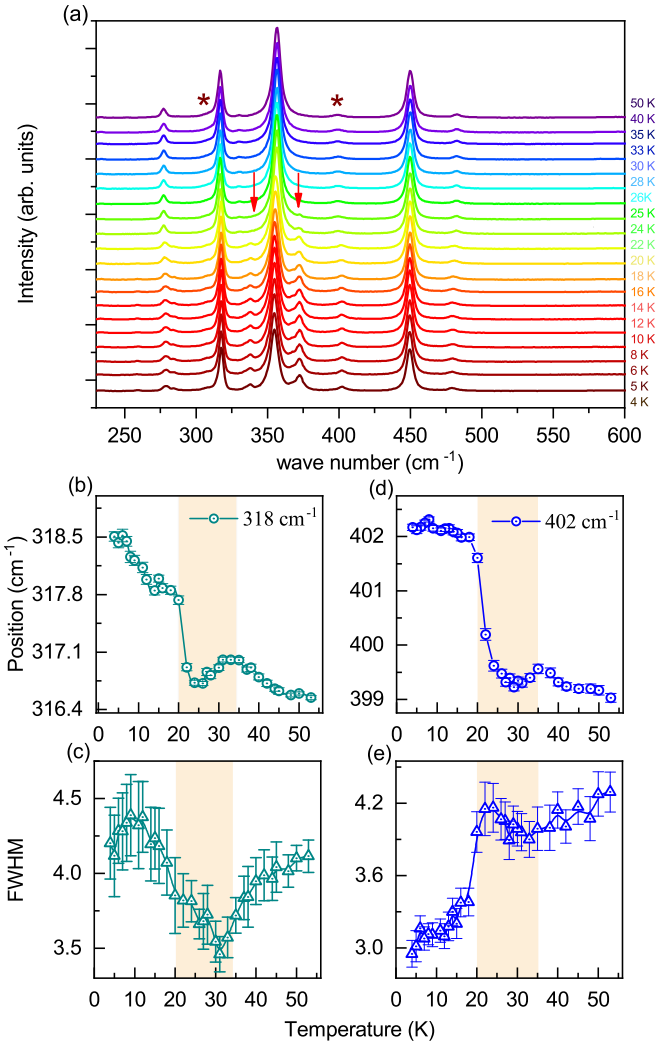


FIG. 2. (a) Temperature-dependent Raman spectra of $Ho_{0.5}Nd_{0.5}Fe_3(BO_3)_4$. Arrows show the appearance of new vibrational modes at ∼337 and ∼372 cm$^{-1}$. Asterisks show visible changes of the 318 cm$^{-1}$ and 402 cm$^{-1}$ modes with temperature. (b, d) Temperature-dependent Raman shifts and the corresponding linewidths (c, e) of 318 cm$^{-1}$ and 402 cm$^{-1}$ modes, respectively.

group analysis data, all these modes are identified as E modes [39,40]. At ∼337 cm$^{-1}$ and ∼372 cm$^{-1}$, new modes appear with decreasing temperature and are much more evident below ∼25 K [marked by an arrow in Fig. 2(a)]. The intensity of new phonon modes in the Raman spectra is mainly associated with atomic displacements ($\delta$) which are related to $I \propto \delta^2$ and are consequences of the appearance of a lower crystal symmetry. The modes ∼318 cm$^{-1}$ and ∼402 cm$^{-1}$ show deviations in both phonon frequencies as well as the FWHM (phonon lifetime) just below $T_N$ [see Figs. 2(b)–2(e)]. Earlier reports explained this peculiarities of phonon modes as a signature of spin-phonon coupling in the AFM phase for ($R$ = Tb, Gd etc.) [41,42]. In the parent compound $HoFe_3(BO_3)_4$, similar changes in Raman vibrational modes were observed both at the structural transition (∼366 K) and at $T_N$ ∼ 38 K, in the high- and low-frequency regions, respectively [40]. Earlier, with partial substitution of Nd in the parent, $HoFe_3(BO_3)_4$ showed significant changes and an appearance of new modes at $T_N$ in the range from 600 to 650 cm$^{-1}$ that were attributed to vibrations of the $BO_3$ triangle [40,43]. These features were explained to arise because of the change in Fe-O-Fe exchange paths, which arises through the magnetoelastic coupling changing the crystal symmetry below $T_N$. However, there was no direct evidence (from structural studies) concerning crystal symmetry change and the correlation of that with electric polarization for those substituted crystals. We would like to emphasize that the appearance of new vibrational modes in this compound at lower frequencies ∼337 cm$^{-1}$ and ∼372 cm$^{-1}$ may belong to the larger structural $FeO_6$ octahedra units. These observed changes in the phonon frequencies reinforce the change in lattice symmetry which is associated with the changes in local atomic positions of the structural unit (affected due to local magnetic interactions) and requires a thorough structural analysis.

### C. Structural evolution studies using synchrotron x-ray diffraction

Although $Ho_{0.5}Nd_{0.5}Fe_3(BO_3)_4$ is reported to possess $R32$ space group (noncentrosymmetric/ nonpolar) down to the lowest temperature, our dielectric and Raman spectroscopic results encourage to carefully investigate the low-temperature crystal structure of this compound. Rietveld refinement of room-temperature SXPD data of this compound confirms the $R32$ space group [see Fig. 3(a)]. We observed discernible changes in peak profiles at lower temperatures. To accurately determine the low-temperature crystal structure, we performed the refinement of SXPD data using $R32$ and $P3_121$ space groups at low temperatures. The weak reflections specifically at higher $2\theta$ values have vital importance in resolving the tiny structural changes [44,45]. At temperatures below $T_N$, for higher $2\theta$ values the resulting intensity profile has better agreement between the observed and calculated intensities for the space group $P3_121$ than $R32$ [Figs. 3(b)–3(d)]. The arrangements of atoms with their atomic positions in $P3_121$ are shown in Fig. 3(e), and the schematic is shown with the changes in atomic positions in the respective space groups in Fig. 3(f). From the temperature-dependent refinement results, we find a steplike compression behavior in lattice parameters and volume across $T_N$ [Figs. 3(g)–3(i)]. Earlier, a similar behavior was reported for a single crystal of $HoFe_3(BO_3)_4$ across the structural transition at ∼366 K [27].

Temperature variations of bond lengths and bond angles in selected polyhedras with major changes are plotted in Figs. 4(a)–4(h). The changes in basal-plane bond lengths are found to be contrasting in nature, which makes the structural units anisotropic. Changes in bond lengths of polyhedras of heavier atoms (e.g., Ho/Nd-O3, Ho/Nd-O7) are less significant across the transition (not shown). The Wyckoff notations and structural parameters obtained for $R32$ (at 50 K) and for $P3_121$ (at 6 K) are presented in Table I. Generally, in the $R32$ phase Fe is positioned at a single site, whereas in the $P3_121$ phase Fe occupies two different sites, Fe1 and Fe2 in the unit cell [27,46]. We found the Ho/Nd-Fe (for both Fe1 and Fe2) bond length to be larger than the intrachain Fe-Fe bond distances in the $FeO_6$ helicoidal chain in the low-temperature phase [Figs. 4(a) and 4(b)]. Hence the intrachain superexchange interaction, i.e., Fe-O-Fe,

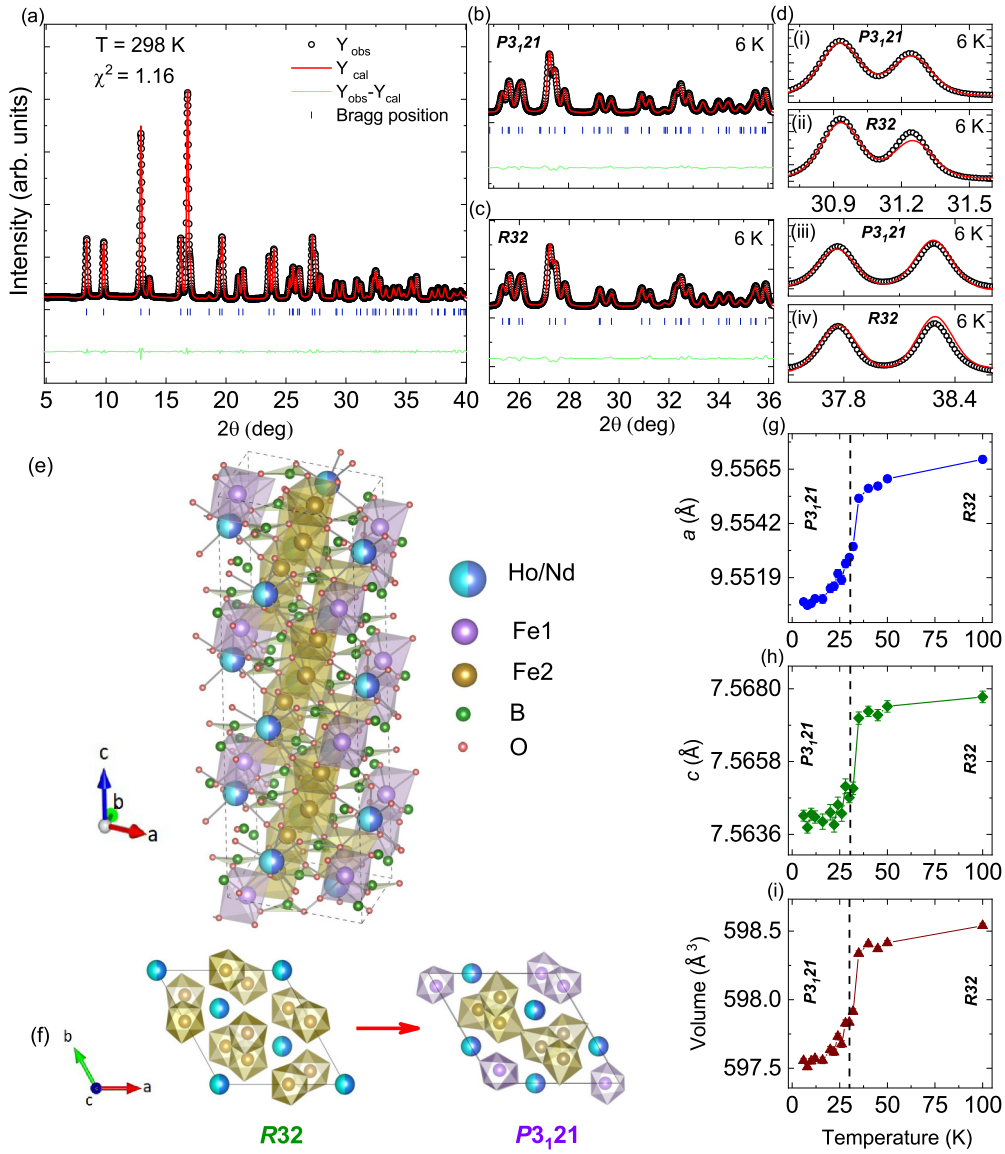


FIG. 3. (a) Rietveld refinement of synchrotron x-ray powder diffraction data of powdered $Ho_{0.5}Nd_{0.5}Fe_3(BO_3)_4$ single crystal at room temperature using the *R*32 space group. (b)–(d) Comparisons of the Rietveld refinements using both $P3_121$ and *R*32 space groups at 6 K. (e) Crystal structure of $P3_121$ and (f) a visual comparison of $P3_121$ and *R*32 unit cells. (g)–(i) Temperature-dependent evolution of lattice parameters and unit-cell volume.

dominates the R(Ho/Nd)-O-Fe interactions. The $B3O_3$ unit doesn't show any distortion with decreasing temperature and remains equilateral (not shown), while for B2-O(O2,O3,O7) and B1-O(O5,O6) the bond lengths change oppositely [see Figs. 4(c) and 4(d)]. The Fe-O interatomic distances in the $Fe1O_6$ and $Fe2O_6$ octahedron in the $P3_121$ phase are very close but behave differently with different oxygen atoms [see Figs. 4(e)–4(g)]. The Fe-O bond distance behaves oppositely for Fe1-O(O3,O6), whereas Fe1-O1 remains unchanged after the phase transition. Significant anisotropic changes have been observed for the $Fe2O_6$ octahedra involving O2 and O5. In a similar study larger changes were observed in $Fe2O_6$ octahedra in $RFe_3(BO_3)_4$ (for *R*= Ho, Gd, Y) at the structural transition [46]. In the $P3_121$ phase, oxygen O2 and O5 each have different positions in the same $Fe2O_6$ octahedra and are also edge shared by the other $Fe2O_6$ in the same chain. Hence, to distinguish better we denoted O2 as (O2′ and O2″) and O5 as (O5′ and O5″), respectively. In the largely distorted $Fe2O_6$ octahedra, in the Fe2-O5″ bond length there is almost no change, while the Fe2-O5′ bond distance decreases to ∼1.84 Å in the low-temperature phase [Fig. 4(e)]. A maximum anisotropic distortion has been observed in Fe2-O2′ (∼1.90 Å) and Fe2-O2″ (∼2.10 Å) of the $Fe2O_6$ unit [Fig. 4(f)]. The above distortions of the $Fe2O_6$ octahedra and the change in Fe-Fe bond distance with decreasing temperature are also accompanied by an increase of the Fe-O-Fe bond angles (Fe2- O2″-Fe2 <Fe2- O5″-Fe2) [Fig. 4(h)].

The above observation of the structural transition is also clearly evident in single crystal x-ray diffraction (SCXD) measurements performed using very-high-brilliance x-rays. Reduction in symmetry that drives the transition is often heralded by weak diffraction peaks (or superlattice reflec-

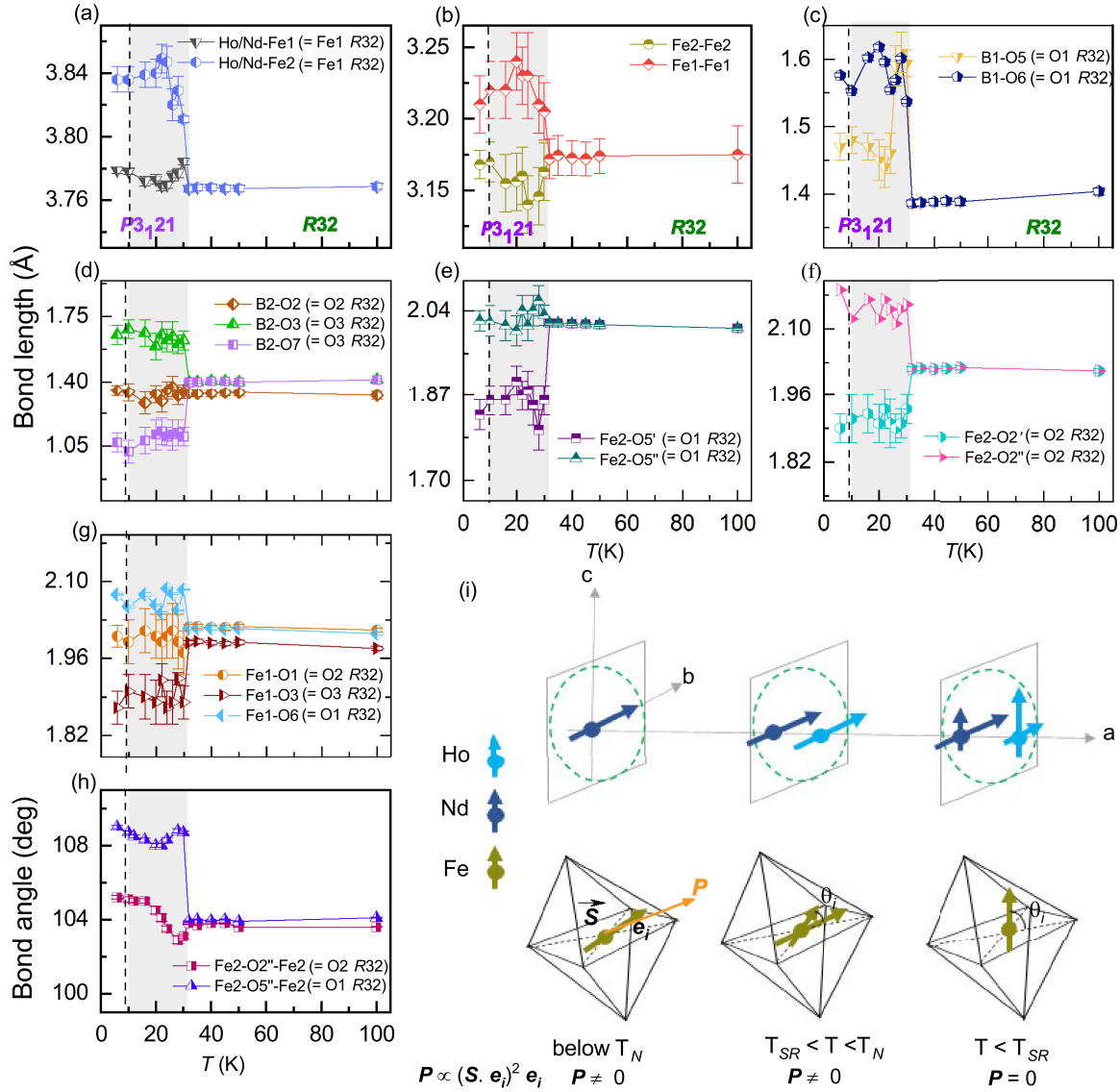


FIG. 4. Temperature-dependent bond lengths were extracted from the Rietveld refinement using both space groups $R32$ (above $T_N$) and $P3_121$ (below $T_N$). (a, b) Ho/Nd-Fe and Fe-Fe bond lengths. Bond lengths of $B1O_3$ and $B2O_3$ triangles are shown in (c, d). (e)–(h) Bond lengths of respective $Fe2O_6$ and $Fe1O_6$ octahedra and Fe-O-Fe bond angles. (i) Schematics of the spins of Ho and Nd ions (top) and Fe spin rotation in the octahedra (bottom) in different temperature regions, below $T_N$, $T_{SR} < T < T_N$, and $T < T_{SR}$. Small and large arrows represent the smaller and larger spin components in the respective crystallographic directions obtained from the XRMS.

tions), which become allowed due to the change in the space group extinction rules. In the $R32$ crystallographic phase, allowed reflections follow the condition $-h + k + l = 3n(D_3^7)$, and for the $P3_121$ condition $l = 3n(D_3^4)$. The (1,2,6) reflection is allowed in $P3_121$ but not in $R32$. The $\theta$-$2\theta$ scans of structural (1,2,6) reflection with varying temperature from 6 to 50 K are shown in Fig. 5(a). The emergence of the (1,2,6) Bragg peak intensity around $T_N$ [see Fig. 5(b)] confirms the spatially symmetry breaking at the onset of magnetic ordering and supports the powder diffraction results.

### D. X-ray resonant magnetic scattering

Undoubtedly, from SXPD and SCXD experiments the structural transition to the $P3_121$ space group at around $T_N$ is confirmed. However, clarity on what is driving the emergence of spontaneous electric polarization below $T_N$ has not been understood. Notwithstanding knowing that spontaneous electric polarization is linked here to magnetism (as in other type-II multiferroics), it is not a trivial task to unravel the exact mechanism because the complex magnetic order in this material (due to the involvement of three different magnetic sublattices Fe, Nd, and Ho) is superimposed on a enantiomorphic chiral structure $P3_121$. Modern synchrotron radiation techniques offer the possibility to utilize hard x-rays as a probe to study the element-specific magnetic structure of magnetic systems and can circumvent this problem. Resonant x-ray magnetic scattering exploits the energy tunability and polarization dependence of incident and diffracted x-rays at third-generation synchrotron sources and allows it to probe the element-specific magnetic structure of magnetic systems. At the resonant condition, polarization-dependent scattering

TABLE I. Refined atomic coordinates and agreement factors of $R32$ (50 K) and $P3_121$ (6 K) space groups from SXPD data.

| $R32$ (50 K) | | | | | $P3_121$ (6 K) | | | | |
|---|---|---|---|---|---|---|---|---|---|
| Atoms | sites | $x$ | $y$ | $z$ | Atoms | sites | $x$ | $y$ | $z$ |
| Ho/Nd | 3*a* | 0.00000 | 0.00000 | 0.00000 | Ho/Nd | 3*a* | 0.66517 | 0.66517 | 0.00000 |
| Fe | 9*d* | 0.55034(11) | 0.00000 | 0.00000 | Fe1 | 3*a* | 0.8822(14) | 0.00000 | 0.33333 |
| O1 | 9*e* | 0.8547(4) | 0.00000 | 0.5 | Fe2 | 6*c* | 0.32968(1) | 0.5489(8) | 0.3447(7) |
| O2 | 9*e* | 0.59418(7) | 0.00000 | 0.5 | O1 | 3*b* | 0.00000 | 0.9317(32) | 0.16666 |
| O3 | 18*f* | 0.02369(4) | 0.2093(4) | 0.18117(5) | O2 | 6*c* | 0.4038(32) | 0.73954 | 0.14642 |
| B1 | 3*b* | 0.00000 | 0.00000 | 0.5 | O3 | 6*c* | 0.7166(23) | 0.8921(25) | 0.1678(33) |
| B2 | 9*e* | 0.4542(11) | 0.00000 | 0.5 | O4 | 6*c* | 0.8622(28) | 0.6391(24) | 0.1989(27) |
| | | | | | O5 | 6*c* | 0.5168(12) | 0.6929(18) | 0.5041(32) |
| | | | | | O6 | 3*b* | 0.80829 | 0.80829 | 0.50000 |
| | | | | | O7 | 6*c* | 0.4829(20) | 0.4566(21) | 0.1798(28) |
| | | | | | B1 | 3*b* | 0.62568 | 0.62568 | 0.50000 |
| | | | | | B2 | 6*c* | 0.5385(34) | 0.8792(41) | 0.1897(44) |
| | | | | | B3 | 3*b* | 0.00000 | 0.8910(48) | 0.16666 |
| | | $a$ (Å) = 9.5560(1) | | | | | $a$ (Å) = 9.5508(1) | | |
| | | $c$ (Å) = 7.5674(2) | | | | | $c$ (Å) = 7.5641(1) | | |
| | | $\chi^2 = 0.893$ | | | | | $\chi^2 = 0.818$ | | |
| | | $R_{wp} = 6.32\%$ | | | | | $R_{wp} = 5.95\%$ | | |
| | | $R_{exp} = 6.69\%$ | | | | | $R_{exp} = 6.57\%$ | | |

can precisely reveal the magnetic moment direction with respect to the scattering plane [47]. The following scattering matrix can be used to infer the magnetic arrangements of the atoms from resonant intensities in the specific polarization channels for electric dipole transitions [48,49]:

$$
\begin{aligned}
&f^{XRES} \\
&= \begin{pmatrix} \sigma\sigma' & \pi\sigma' \\ \sigma\pi' & \pi\pi' \end{pmatrix} = F^{(0)} \begin{pmatrix} 1 & 0 \\ 0 & \cos 2\theta \end{pmatrix} \\
&\quad - iF^{(1)} \begin{pmatrix} 0 & z_1 \cos\theta + z_3 \sin\theta \\ z_3 \sin\theta - z_1 \cos\theta & -z_2 \sin 2\theta \end{pmatrix} \\
&\quad + F^{(2)} \begin{pmatrix} z_2^2 & z_2(z_1 \sin\theta - z_3 \cos\theta) \\ z_2(z_1 \sin\theta + z_3 \cos\theta) & -\cos^2\theta\left(z_1^2 \tan^2\theta + z_3^2\right) \end{pmatrix}.
\end{aligned}
$$

Here, $\theta$ is the scattering angle, and $z_1$, $z_2$, $z_3$ are the components of magnetic moments along $u_1$, $u_2$, and $u_3$ [see Figs. 6(a) and 6(b)]. $z_3$ is the moment direction antiparallel to the scattering vector, $z_2$ is the moment perpendicular to the scattering plane, and $z_1$ is perpendicular to these two. The first matrix describes pure charge scattering, whereas the second and third matrix describe the first-harmonic and second-harmonic magnetic satellites, respectively. The quadratic component (third matrix) is usually very weak, has a complex polarization dependence, and can be ignored. The second matrix describes magnetic components observed in $\sigma\pi'$, $\pi\pi'$, and $\pi\sigma'$ polarization channels. By appropriately choosing the scattering plane and polarization channels, these magnetic signals can be identified. In the vertical scattering geometry ($\sigma$-incident polarization), the rotated polarization channel ($\sigma\pi'$) provides information on the magnetic components lying in the scattering plane, i.e., (*ac* plane). In the horizontal scattering geometry ($\pi$-incident polarization), the rotated channel ($\pi\sigma'$) and unrotated channel ($\pi\pi'$) probe magnetic components lying in the scattering plane, i.e., *ac* plane, and perpendicular to the scattering plane, i.e., along *b* direction, respectively.

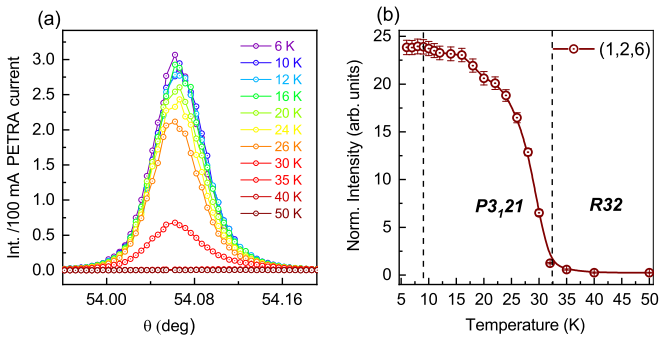


FIG. 5. (a) Temperature dependence of $\theta$ scans of (1,2,6) Bragg peak (forbidden in $R32$ space group). (b) Integrated intensity vs temperature for the (1,2,6) reflection.

For insights of magnetic ordering of all three atoms, XRMS at zero magnetic field across the *L* edges of Nd and Ho atoms and across the *K* edge of the Fe atom has been performed in both the vertical and horizontal geometry. Figures 6(a) and 6(b) show the schematics of both the vertical ($\sigma$-incidence) and horizontal ($\pi$-incidence) scattering geometries. Energy scans of the magnetic (0,0,7.5) reflection across the absorption edges (along with the respective fluorescence energy scans) and temperature dependence of resonant intensities of all three atoms in both channels ($\sigma\pi'$ & $\pi\pi'$) are shown in Figs. 6(c)–6(k).

The intensity behavior of the magnetic (0,0,7.5) reflection at the Fe *K* edge in the $\sigma\pi'$ channel represents the net induced Fe moments in the *ac* plane below $T_N$ which grows up to 4 K [Fig. 6(f)]. However, the anomaly observed in between 25 and 15 K indicates a partial rotation of the Fe moments into the *ac* plane. The behavior in the $\pi\pi'$ channel is different, and the Fe *K*-edge resonant intensity shows that the Fe moments order spontaneously from 32 to 10 K along the *b* direction

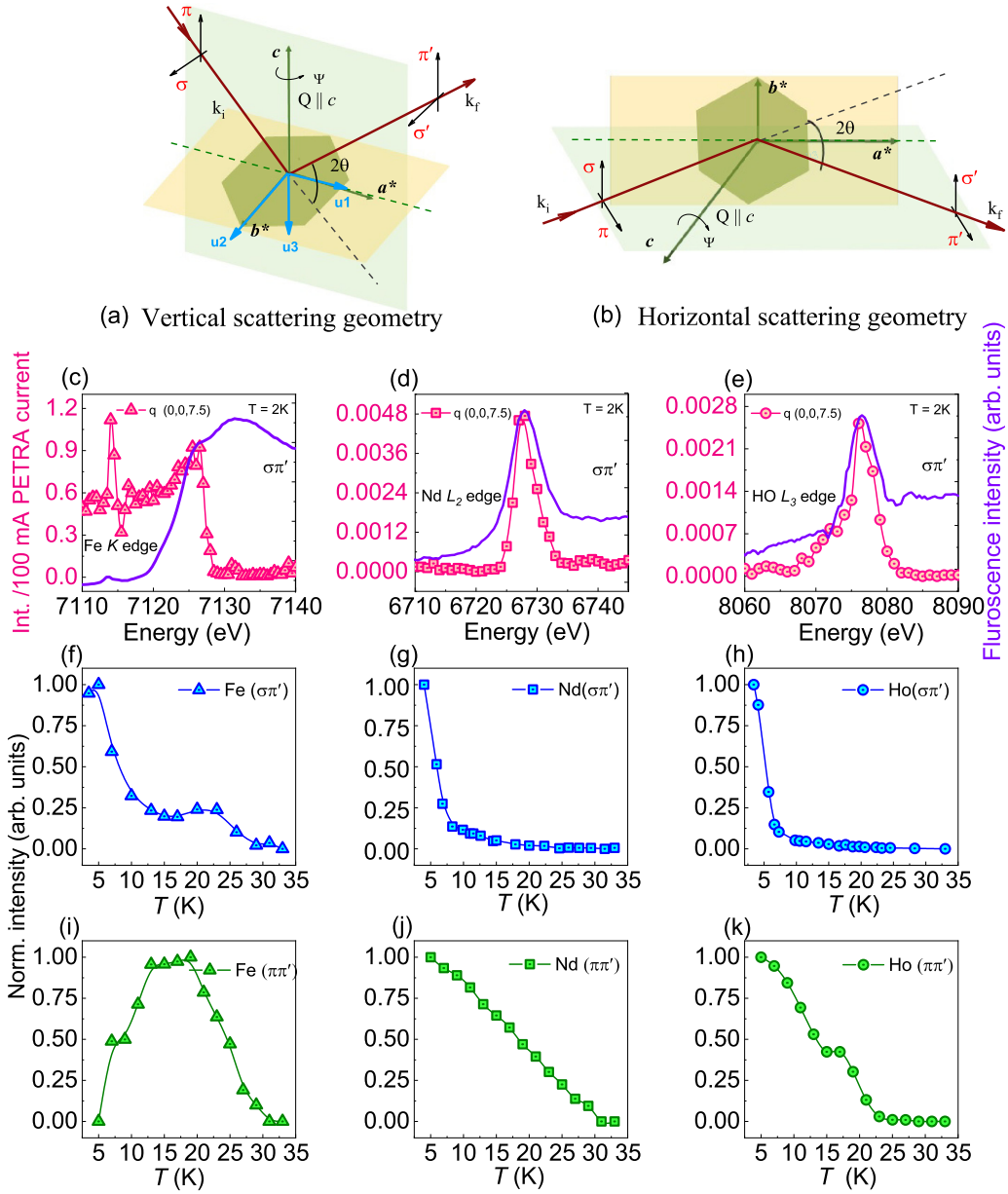


FIG. 6. (a, b) Schematics of vertical and horizontal scattering geometries of x-ray resonant magnetic scattering, respectively. (c)–(e) Energy scans across the Fe-$K$ edge, Nd-$L_2$ edge, and Ho-$L_3$ edge at the magnetic (0,0,7.5) reflection measured in $\sigma\pi'$ channel at 2 K. The solid lines (in violet) are the fluorescence energy scans across the respective edges. (f)–(k) Temperature dependence of the integrated intensities of the magnetic (0,0,7.5) reflection at zero magnetic field measured in the $\sigma\pi'$ and $\pi\pi'$ channels, extracted from $L$ scans.

(rise at ∼25 K). The drop in intensity below $T_{SR}$ ∼ 9 K signifies that the Fe moments are no longer oriented along the $b$ axis [Fig. 6(i)]. These observations show that below $T_N$ the Fe moments originally order with a strong component along the $b$ direction ($\pi\pi'$ channel), although having small $ac$-plane components and below $T_{SR}$ completely rotate into the $ac$ plane ($\sigma\pi'$ channel), which shows a collinear spin arrangement of Fe below $T_{SR}$. At the Nd-$L_2$ edge, the intensity of the magnetic (0,0,7.5) reflection emerging below $T_N$ represents spontaneous ordering behavior appearing in the $\pi\pi'$ channel and induced behavior in the $\sigma\pi'$ channel [Figs. 6(g) and 6(j)]. This means the Nd moment is directed predominantly in the $b$ direction and starts to order at the onset of $T_N$. Below $T_{SR}$, a sharp increase of intensity (∼6 K) in the $\sigma\pi'$ channel indicates the appearance of a component of the Nd moments also in the $ac$ plane. At the Ho-$L_3$ edge, the intensity in the $\pi\pi'$ channel starts to appear below ∼25 K (with partial rotation of the Fe moments into the $ac$ plane) and also there, a sharp increase of the $\sigma\pi'$ intensity below $T_{SR}$ is observed [Figs. 6(h) and 6(k)]. The Nd moments along the $b$ direction order concomitantly with Fe at $T_N$, while Ho moments start to order at slightly lower temperature (∼25 K). These results indicate that the onset of the AFM ordering is governed mainly by the Fe-O-Fe superexchange interaction (and sets-in in the basal plane $ab$ plane). Ordering of the Fe moments assists in the orderings of the Ho and Nd moments along the $b$ direction as well, although it is reported that Nd and Ho have distinct anisotropies, easy plane and easy axis, respectively [30,31].

Below $T_{SR}$, all three moments adopt easy-axis anisotropy and align along the *ac* plane, which could be due to the strong influence of easy-axis anisotropy of Ho on the ordering of Fe and Nd, at very low temperatures. The nonzero intensity in the $\pi\pi'$ channel for both Ho and Nd below $T_{SR}$ attribute to the noncollinear spin arrangement. Spontaneous polarization ($\boldsymbol{P}_{ab}$) can be correlated directly with the Fe ordering behavior, which arises below $T_N$ and drops at $T_{SR}$. It is therefore apparent that the Fe ordering plays a significant role in the multiferroic behavior of this compound.

## IV. DISCUSSIONS

Significant changes in the lattice parameters and unit-cell volume at ∼32 K obtained from SXPD gave evidence of structural transition (from $R32$ to $P3_121$) at the onset of magnetic ordering, $T_N$. The systematic appearance of the (1,2,6) Bragg peak below $T_N$ in SCXD further confirmed the symmetry lowering and transition into the $P3_121$ space group. Findings of structural investigations are well corroborated with the dielectric spectroscopy, Raman spectroscopy, and pyrocurrent measurements. The observed changes in the Raman spectroscopy at $T_N$, both in phonon frequencies and FWHM, may be due to the modulation in Fe-O-Fe exchange interaction contributions through the spin-phonon coupling, as Raman is sensitive to lattice modulation and is thus susceptible to these changes across magnetic transitions. Earlier structural studies on the type-II multiferroics, such as $TbMn_2O_5$, $NdCrTiO_5$, etc., have confirmed the change from centrosymmetric to noncentrosymmetric space group (nonpolar to polar) at magnetic transitions, where the spontaneous polarization sets-in clearly due to change in symmetry [6,50,51]. In the present case, $Ho_{0.5}Nd_{0.5}Fe_3(BO_3)_4$ is nonpolar as well as noncentrosymmetric in the high-temperature phase ($R32$) and does not exhibit spontaneous electric polarization. With the onset of magnetic ordering at low temperature it transitions into $P3_121$, which is also noncentrosymmetric but belongs to a enantiomorphic chiral space group [52,53].

There are three different mechanisms describing the emergence of spontaneous electric polarization in magnetic multiferroics, namely, symmetric exchange striction, inverse Dzyaloshinskii–Moriya (DM) interaction (spin-current model), and spin-dependent *p-d* hybridization [54–60]. In the case of symmetric exchange striction, neighboring spins $S_i$ and $S_j$ have spin arrangements as ↑↑↓↓ (dimer singlet formation). For macroscopic polarization ($P$), the spin modulation should be commensurate with the crystal lattice producing induced striction along a specific crystallographic direction $\Pi_{ij} \propto (\boldsymbol{S}_i \cdot \boldsymbol{S}_j)$ [61]. From the XRMS results, it is found that below $T_N$ the Fe spins have noncollinear arrangements [Fig. 4(i)]. It is also known that the exchange interaction is more prominent for Fe-O-Fe (intrachain interaction at $T_N$), as the R-O-B-O-R exchange path is very weak. Hence it is more probable to produce striction along the *c* direction, which cannot be the case for the observed polarization ($\boldsymbol{P}_{ab}$). Moreover, from SXPD results, there are anisotropic changes observed in most of the bond lengths of polyhedra, which further discards the striction mechanism for the emergence of $\boldsymbol{P}_{ab}$. Next comes the spin-current model, which requires spiral spin configuration (cycloidal) to produce polarization $\boldsymbol{P} \propto \boldsymbol{e}_{ij} \times (\boldsymbol{S}_i \times \boldsymbol{S}_j)$ between the canted spins $\boldsymbol{S}_i$ and $\boldsymbol{S}_j$, with $\boldsymbol{e}_{ij}$ being the unit vector connecting the sites $i$ and $j$, as described in $TbMnO_3$ [57]. In this model, as a consequence of inverse DM interaction an intervening ligand atom between rotating spins is displaced and a finite polarization is introduced in the direction perpendicular to spin rotation axis and magnetic propagation vector [62]. In the studied compound there are edge-shared $FeO_6$ octahedra and almost all the ligand oxygen atoms are found to displace below $T_N$, causing an overall anisotropic distortion in $FeO_6$ octahedra which cannot explain $\boldsymbol{P}_{ab}$. In the present case the polarization ($\boldsymbol{P}_{ab}$) can be most suitably explained by invoking the *p-d* hybridization mechanism, which involves rotation of a single magnetic ion (Fe spin) inside the octahedron ($FeO_6$). The covalency between metal $d$ and ligand $p$ orbitals is modulated depending on the local spin moment direction via spin-orbit interaction, and the local electric dipole is produced, i.e., polarization $\Delta\boldsymbol{P} \propto (\boldsymbol{S} \cdot \boldsymbol{e}_i)^2 \boldsymbol{e}_i \propto (\boldsymbol{S} \cos\theta_i)^2 \boldsymbol{e}_i$ arises along the metal-ligand bond direction [60], where $\boldsymbol{e}_i$ is the vector connecting the metal (here Fe) and $i$th ligand O ion, and $\theta_i$ is the angle between spin and $\boldsymbol{e}_i$, respectively [see Fig. 4(i), which is based on XRMS results]. While in most cases this term oscillates and cancels out within a crystal, the appropriate combination of spin configuration and crystallographic lattice can avoid the cancellation and cause macroscopic electric polarization ($P$). Such a mechanism was well explained in a tetragonal antiferromagnet $Ba_2CoGe_2O_7$, which is also nonpolar and noncentrosymmetric [60]. The polarization emergence was attributed to spin-dependent *p-d* hybridization where the local dipole moment was induced with the Co spin moment within the $CoO_4$ tetrahedron.

Earlier, a quantum theory of the magnetoelectric effect in the $RFe_3(BO_3)_4$ ($R$ = Nd, Sm, Eu) explained by the two single-ion mechanisms, i.e., electronic (electric dipole moment due to the electronic 4$f$ shell with the combined crystal field and exchange field) and ionic (displacement of oppositely charged sublattices in a magnetic field) [63]. Also, for the $R$ = Gd, Eu, Tb compounds, multiferroicity was explained as originating from spin-dependent *p-d* hybridization, which was understood from the point of view of symmetry of Fe sites [18]. In the $P3_121$ phase of $Ho_{0.5}Nd_{0.5}Fe_3(BO_3)_4$ there are two Fe sites (Fe1:Fe2 = 1:2) in the helicoidal chains along the *c* axis yielding two threefold screw ($3_1$) symmetry axes in the unit cell. For nonzero polarization, spin order with a lower symmetry is crystallographically more preferable, because due to the spin order the lower symmetry may easily create a polar state in a nonpolar crystallographic lattice. From our structural analysis we found a net clear change in the metal-ligand (Fe-O) bond lengths in the distorted $FeO_6$ octahedra at low-temperature phase. The anisotropic bond length change can be compared with the Fe spin ordering (although XRMS cannot distinguish different Fe sites) as it starts to order below $T_N$ (mostly along the *b* axis) [Fig. 6(i)]. Hence the polarization appearance below $T_N$ is related to the formation of local dipole moments (spin-induced dipoles). During the rise in the $\boldsymbol{P}_{ab}$ at ∼25 K ($T_{SR} < T < T_N$), most of the Fe spins are aligned along the *b* axis, although a small component is found along the *ac* plane. The sudden drop in the $\boldsymbol{P}_{ab}$ occurring below $T_{SR}$ is due to the Fe spin reorientation transition, i.e., of Fe spin components rotating completely from *b* axis into the

*ac* plane [Fig. 6(f)] due to strong easy-axis (*c* axis) anisotropy of the Ho. Below $T_{SR}$ the Fe spins behave as collinear arrangement along the *c* axis. Similar collinear Fe spin arrangement has been reported for $HoFe_3(BO_3)_4$ at 2 K ($T_{SR} \sim 5$ K) [8]. Hence the opposite spin arrangements may cause the cancellation of dipole moments of opposite directions, resulting a gradual decrease in net polarization ($\boldsymbol{P}_{ab}$). Moreover, from the XRMS study at the Nd-$L_2$ edge, we found magnetic components in the *ac* plane below the $T_{SR}$. This shows contrasting behavior, although it depicts an easy-plane anisotropy. Hence, the 50% Nd substitution in the $Ho_{0.5}Nd_{0.5}Fe_3(BO_3)_4$ may be playing a significant role in stabilizing structure and in the increase of the spontaneous polarization as compared to the parent compounds. A comparative study of the detailed structural and magnetic structure information of all the Nd-doped compounds would be required (which are scarcely available in the literature) to understand the role of ordered Nd ion sublattice in spontaneous polarization. The observation of subtle structural changes at low temperature and element-specific magnetic ordering behavior allow a new understanding of the emergence of spontaneous polarization in this family of compounds.

## V. CONCLUSIONS

In conclusion, we have performed a comprehensive structural study of $Ho_{0.5}Nd_{0.5}Fe_3(BO_3)_4$ by SXPD and SCXD experiments which provides evidence of lowering of crystallographic symmetry at the onset of magnetic ordering. The dielectric and Raman spectroscopy studies corroborate well with the structural transition. XRMS study provides information of magnetic ordering behavior of all three magnetic sublattices (Fe, Ho, and Nd) up to lowest temperature. We observe a collinear spin arrangement for the Fe and a noncollinear spin arrangement for the Ho and the Nd below the spin reorientation transition temperature. Our results show that the spontaneous polarization follows the rotation of the Fe spin from the *b*-axis towards the *ac*-plane. The spontaneous electric polarization below AFM in $Ho_{0.5}Nd_{0.5}Fe_3(BO_3)_4$ arises due to the formation of a local electric dipole moment by the combined effect of lowering of local symmetry of the $FeO_6$ octahedra and Fe spin rotation and can be understood through the spin-dependent *p-d* hybridization mechanism. Overall, our study of $Ho_{0.5}Nd_{0.5}Fe_3(BO_3)_4$ envisions the origin of the emergence of spontaneous electric polarization and manifests a valuable insight into the magnetic and structural interplay of the rare-earth borate compounds.

## ACKNOWLEDGMENTS

A.T. and D.K.S. gratefully acknowledge financial support from the Department of Science and Technology (DST) in India for travel support through the India-DESY Collaboration for performing experiments at PETRA-III, DESY. D.K.S. acknowledges support from the DST, New Delhi, India, through Grant No. INI/RUS/RFBR/P-269 (DST-RSF project). The authors acknowledge K. Sharma for help during magnetization measurements.

[1] T. Kimura, T. Goto, H. Shintani, K. Ishizaka, T.-h. Arima, and Y. Tokura, Magnetic control of ferroelectric polarization, Nature (London) **426**, 55 (2003).

[2] R. Ramesh, Emerging routes to multiferroics, Nature (London) **461**, 1218 (2009).

[3] N. A. Spaldin, S.-W. Cheong, and R. Ramesh, Multiferroics: Past, present, and future, Phys. Today **63**(10), 38 (2010).

[4] T. Kimura, J. Lashley, and A. Ramirez, Inversion-symmetry breaking in the noncollinear magnetic phase of the triangular-lattice antiferromagnet $CuFeO_2$, Phys. Rev. B **73**, 220401(R) (2006).

[5] S. Picozzi, K. Yamauchi, B. Sanyal, I. A. Sergienko, and E. Dagotto, Dual Nature of Improper Ferroelectricity in a Magnetoelectric Multiferroic, Phys. Rev. Lett. **99**, 227201 (2007).

[6] K. Gautam, A. Ahad, K. Dey, S. S. Majid, S. Francoual, V. G. Sathe, I. da Silva, and D. K. Shukla, Symmetry breaking and spin lattice coupling in $NdCrTiO_5$, Phys. Rev. B **100**, 104106 (2019).

[7] S.-W. Cheong and M. Mostovoy, Multiferroics: A magnetic twist for ferroelectricity, Nat. Mater. **6**, 13 (2007).

[8] C. Ritter, A. Vorotynov, A. Pankrats, G. Petrakovskii, V. Temerov, I. Gudim, and R. Szymczak, Magnetic structure in iron borates $RFe_3(BO_3)_4$ (R = Y, Ho): A neutron diffraction and magnetization study, J. Phys.: Condens. Matter **20**, 365209 (2008).

[9] H. Mo, C. S. Nelson, L. N. Bezmaternykh, and V. T. Temerov, Magnetic structure of the field-induced multiferroic $GdFe_3(BO_3)_4$, Phys. Rev. B **78**, 214407 (2008).

[10] R. P. Chaudhury, F. Yen, B. Lorenz, Y. Y. Sun, L. N. Bezmaternykh, V. L. Temerov, and C.-W. Chu, Magnetoelectric effect and spontaneous polarization in $HoFe_3(BO_3)_4$ and $Ho_{0.5}Nd_{0.5}Fe_3(BO_3)_4$, Phys. Rev. B **80**, 104424 (2009).

[11] U. Adem, L. Wang, D. Fausti, W. Schottenhamel, P. H. van Loosdrecht, A. Vasiliev, L. N. Bezmaternykh, B. Büchner, C. Hess, and R. Klingeler, Magnetodielectric and magnetoelastic coupling in $TbFe_3(BO_3)_4$, Phys. Rev. B **82**, 064406 (2010).

[12] J. Hamann-Borrero, M. Philipp, O. Kataeva, M. v. Zimmermann, J. Geck, R. Klingeler, A. Vasiliev, L. Bezmaternykh, B. Büchner, and C. Hess, Nonresonant x-ray magnetic scattering on rare-earth iron borates $RFe_3(BO_3)_4$, Phys. Rev. B **82**, 094411 (2010).

[13] D. K. Shukla, S. Francoual, A. Skaugen, M. v. Zimmermann, H. Walker, L. N. Bezmaternykh, I. A. Gudim, V. L. Temerov, and J. Strempfer, Ho and Fe magnetic ordering in multiferroic $HoFe_3(BO_3)_4$, Phys. Rev. B **86**, 224421 (2012).

[14] T. Stanislavchuk, E. Chukalina, M. Popova, L. Bezmaternykh, and I. Gudim, Investigation of the iron borates $DyFe_3(BO_3)_4$ and $HoFe_3(BO_3)_4$ by the method of $Er^{3+}$ spectroscopic probe, Phys. Lett. A **368**, 408 (2007).

[15] M. N. Popova, E. P. Chukalina, T. N. Stanislavchuk, B. Z. Malkin, A. R. Zakirov, E. Antic-Fidancev, E. A. Popova, L. N. Bezmaternykh, and V. L. Temerov, Optical spectra, crystal-field parameters, and magnetic susceptibility of multiferroic $NdFe_3(BO_3)_4$, Phys. Rev. B **75**, 224435 (2007).

[16] M. Popova, Optical spectroscopy of low-dimensional rare-earth iron borates, J. Magn. Magn. Mater. **321**, 716 (2009).

[17] J. Hamann-Borrero, S. Partzsch, S. Valencia, C. Mazzoli, J. Herrero-Martin, R. Feyerherm, E. Dudzik, C. Hess, A. Vasiliev, L. Bezmaternykh *et al.*, Magnetic Frustration, Phase Competition, and the Magnetoelectric Effect in $NdFe_3(BO_3)_4$, Phys. Rev. Lett. **109**, 267202 (2012).

[18] T. Kurumaji, K. Ohgushi, and Y. Tokura, Magnetoelectric responses from the respective magnetic *R* and Fe subsystems in the noncentrosymmetric antiferromagnets $RFe_3(BO_3)_4$ (*R*=Eu, Gd, and Tb), Phys. Rev. B **89**, 195126 (2014).

[19] H. Nakajima, T. Usui, Y. Joly, M. Suzuki, Y. Wakabayashi, T. Kimura, and Y. Tanaka, Quadrupole moments in chiral material $DyFe_3(BO_3)_4$ observed by resonant x-ray diffraction, Phys. Rev. B **93**, 144116 (2016).

[20] A. Malakhovskii, A. Sukhachev, A. Leont'ev, I. Gudim, A. Krylov, and A. Aleksandrovsky, Spectroscopic properties of $Nd_{0.5}Gd_{0.5}Fe_3(BO_3)_4$ single crystal, J. Alloys Compd. **529**, 38 (2012).

[21] J. Campa, C. Cascales, E. Gutierrez-Puebla, M. Monge, I. Rasines, and C. Ruiz-Valero, Crystal structure, magnetic order, and vibrational behavior in iron rare-earth borates, Chem. Mater. **9**, 237 (1997).

[22] H. Zhang, S. Liu, C. S. Nelson, L. Bezmaternykh, Y. Chen, S. Wang, R. Lobo, K. Page, M. Matsuda, D. Pajerowski *et al.*, Structural features associated with multiferroic behavior in the $RX_3(BO_3)_4$ system, J. Phys.: Condens. Matter **31**, 505704 (2019).

[23] A. Vasiliev and E. Popova, Rare-earth ferroborates $RFe_3(BO_3)_4$, Low Temp. Phys. **32**, 735 (2006).

[24] D. Volkov, A. Demidov, and N. Kolmakova, Magnetic properties of an easy-plane trigonal $NdFe_3(BO_3)_4$ antiferromagnet, J. Exp. Theor. Phys. **104**, 897 (2007).

[25] A. Kadomtseva, Y. F. Popov, G. Vorob'ev, A. Pyatakov, S. Krotov, K. Kamilov, V. Y. Ivanov, A. Mukhin, A. Zvezdin, A. Kuz'menko *et al.*, Magnetoelectric and magnetoelastic properties of rare-earth ferroborates, Low Temp. Phys. **36**, 511 (2010).

[26] A. A. Mukhin, G. P. Vorob'ev, V. Y. Ivanov, A. M. Kadomtseva, A. Narizhnaya, A. Kuz'menko, Y. F. Popov, L. N. Bezmaternykh, and I. Gudim, Colossal magnetodielectric effect in $SmFe_3(BO_3)_4$ multiferroic, JETP Lett. **93**, 275 (2011).

[27] E. S. Smirnova, O. A. Alekseeva, A. P. Dudka, D. Khmelenin, K. V. Frolov, M. V. Lyubutina, I. A. Gudim, and I. S. Lyubutin, Crystal structure and structural phase transition in bismuth-containing $HoFe_3(BO_3)_4$ in the temperature range 11–500 K, Acta Crystallogr., Sect. B: Struct. Sci., Cryst. Eng. Mater. **75**, 954 (2019).

[28] A. Tripathy, K. Gautam, K. Dey, A. Ahad, I. Gudim, V. Sathe, and D. Shukla, Dielectric and Raman spectroscopy measurements across structural phase transition in multiferroic $HoFe_3(BO_3)_4$ single crystal, in *Proceedings of the International Conference on Advanced Materials: ICAM 2019*, AIP Conf. Proc. No. 2162 (AIP Publishing LLC, Melville, NY, 2019), p. 020062.

[29] R. Chaudhury, B. Lorenz, Y. Sun, L. Bezmaternykh, V. Temerov, and C. Chu, Magnetic phase diagram and magnetoelectric properties of $Ho_{0.25}Nd_{0.75}Fe_3(BO_3)_4$, J. Appl. Phys. **107**, 09D913 (2010).

[30] P. Fischer, V. Pomjakushin, D. Sheptyakov, L. Keller, M. Janoschek, B. Roessli, J. Schefer, G. Petrakovskii, L. Bezmaternikh, V. Temerov *et al.*, Simultaneous antiferromagnetic $Fe^{3+}$ and $Nd^{3+}$ ordering in $NdFe_3(B_{11}O_3)_4$, J. Phys.: Condens. Matter **18**, 7975 (2006).

[31] M. Platunov, N. Kazak, V. Dudnikov, V. Temerov, I. Gudim, Y. Knyazev, S. Gavrilkin, V. Dyadkin, I. Dovgaliuk, D. Chernyshov *et al.*, Element selective magnetism in $Ho_{0.5}Nd_{0.5}Fe_3(BO_3)_4$ single crystal probed with hard x-ray magnetic circular dichroism, J. Magn. Magn. Mater. **479**, 312 (2019).

[32] I. Gudim, A. Demidov, E. Eremin, and D. Shukla, Magnetic and magnetodielectric properties of $Ho_{0.5}Nd_{0.5}Fe_3(BO_3)_4$, Phys. Solid State **60**, 1989 (2018).

[33] M. Popova, E. Chukalina, D. Erofeev, I. Gudim, I. Golosovsky, A. Gukasov, A. Mukhin, and B. Malkin, High-resolution optical spectroscopy, magnetic properties, and single-crystal neutron diffraction of multiferroic $HoFe_3(BO_3)_4$: Magnetic structure, Phys. Rev. B **103**, 094411 (2021).

[34] A. K. Zvezdin, G. P. Vorob'ev, A. M. Kadomtseva, Y. F. Popov, A. P. Pyatakov, L. N. Bezmaternykh, A. Kuvardin, and E. Popova, Magnetoelectric and magnetoelastic interactions in $NdFe_3(BO_3)_4$ multiferroics, JETP Lett. **83**, 509 (2006).

[35] J. Rodríguez-Carvajal, Recent advances in magnetic structure determination by neutron powder diffraction, Phys. B: Condens. Matter **192**, 55 (1993).

[36] K. Momma and F. Izumi, Vesta 3 for three-dimensional visualization of crystal, volumetric and morphology data, J. Appl. Crystallogr. **44**, 1272 (2011).

[37] J. Strempfer, S. Francoual, D. Reuther, D. K. Shukla, A. Skaugen, H. Schulte-Schrepping, T. Kracht, and H. Franz, Resonant scattering and diffraction beamline P09 at PETRA III, J. Synchrotron Radiat. **20**, 541 (2013).

[38] R. Levitin, E. Popova, R. Chtsherbov, A. N. Vasiliev, M. N. Popova, E. P. Chukalina, S. A. Klimin, P. Van Loosdrecht, D. Fausti, and L. N. Bezmaternykh, Cascade of phase transitions in $GdFe_3(BO_3)_4$, J. Exp. Theor. Phys. Lett. **79**, 423 (2004).

[39] D. Fausti, A. A. Nugroho, P. H. van Loosdrecht, S. A. Klimin, M. N. Popova, and L. N. Bezmaternykh, Raman scattering from phonons and magnons in $RFe_3(BO_3)_4$, Phys. Rev. B **74**, 024403 (2006).

[40] A. Krylov, S. Sofronova, I. Gudim, S. Krylova, R. Kumar, and A. Vtyurin, Manifestation of magnetoelastic interactions in Raman spectra of $Ho_{1-x}Nd_xFe_3(BO_3)_4$ crystals, J. Adv. Dielect. **08**, 1850011 (2018).

[41] M. Popova, K. Boldyrev, S. Klimin, T. Stanislavchuk, A. Sirenko, and L. Bezmaternykh, Spectral signatures of spin–phonon and electron–phonon interactions in multiferroic iron borates, J. Magn. Magn. Mater. **383**, 250 (2015).

[42] S. Klimin, A. Kuzmenko, M. Kashchenko, and M. Popova, Infrared study of lattice dynamics and spin-phonon and electron-phonon interactions in multiferroic $NdFe_3(BO_3)_4$ and $GdFe_3(BO_3)_4$, Phys. Rev. B **93**, 054304 (2016).

[43] A. S. Krylov, S. N. Sofronova, I. A. Gudim, and A. N. Vtyurin, Magnetoelastic interactions in Raman spectra of $Ho_{1-x}Nd_xFe_3(BO_3)_4$ crystals, Solid State Commun. **174**, 26 (2013).

[44] R. E. Marsh, The importance of weak reflections in resolving the centrosymmetric-noncentrosymmetric ambiguity: A cautionary tale, Acta Crystallogr., Sect. B: Struct. Sci., Cryst. Eng. Mater. **37**, 1985 (1981).

[45] R. E. Marsh, Centrosymmetric or noncentrosymmetric?, Acta Crystallogr. Sect. B: Struct. Sci. **42**, 193 (1986).

[46] O. A. Alekseeva, E. S. Smirnova, K. V. Frolov, M. V. Lyubutina, I. S. Lyubutin, and I. A. Gudim, Crystal structure dynamics of $RFe_3(BO_3)_4$ single crystals in the temperature range 25–500 K, Crystals **12**, 1203 (2022).

[47] J. Hannon, G. Trammell, M. Blume, and D. Gibbs, X-Ray Resonance Exchange Scattering, Phys. Rev. Lett. **61**, 1245 (1988).

[48] T. Brückel, M. Lippert, T. Köhler, J. Schneider, W. Prandl, V. Rilling, and M. Schilling, The non-resonant magnetic x-ray scattering cross section of $MnF_2$, 1. Medium x-ray energies from 5 to 12 keV, Acta Crystallogr., Sect. A: Found. Crystallogr. **52**, 427 (1996).

[49] J. Hill and D. McMorrow, Resonant exchange scattering: Polarization dependence and correlation function, Acta Crystallogr., Sect. A: Found. Crystallogr. **52**, 236 (1996).

[50] N. Narayanan, P. Graham, P. Rovillain, J. O'Brien, J. Bertinshaw, S. Yick, J. Hester, A. Maljuk, D. Souptel, B. Büchner *et al.*, Reduced crystal symmetry as the origin of the ferroelectric polarization within the incommensurate magnetic phase of $TbMn_2O_5$, Phys. Rev. B **105**, 214413 (2022).

[51] V. Balédent, S. Chattopadhyay, P. Fertey, M. Lepetit, M. Greenblatt, B. Wanklyn, F. Saouma, J. Jang, and P. Foury-Leylekian, Evidence for Room Temperature Electric Polarization in $RMn_2O_5$ Multiferroics, Phys. Rev. Lett. **114**, 117601 (2015).

[52] R. Johnson, K. Cao, L. Chapon, F. Fabrizi, N. Perks, P. Manuel, J. Yang, Y. S. Oh, S.-W. Cheong, and P. Radaelli, $MnSb_2O_6$: A Polar Magnet with a Chiral Crystal Structure, Phys. Rev. Lett. **111**, 017202 (2013).

[53] T. Usui, Y. Tanaka, H. Nakajima, M. Taguchi, A. Chainani, M. Oura, S. Shin, N. Katayama, H. Sawa, Y. Wakabayashi *et al.*, Observation of quadrupole helix chirality and its domain structure in $DyFe_3(BO_3)_4$, Nat. Mater. **13**, 611 (2014).

[54] Y. Tokura, S. Seki, and N. Nagaosa, Multiferroics of spin origin, Rep. Prog. Phys. **77**, 076501 (2014).

[55] S. Ishiwata, Y. Kaneko, Y. Tokunaga, Y. Taguchi, T.-h. Arima, and Y. Tokura, Perovskite manganites hosting versatile multiferroic phases with symmetric and antisymmetric exchange strictions, Phys. Rev. B **81**, 100411(R) (2010).

[56] G. Lawes, A. B. Harris, T. Kimura, N. Rogado, R. J. Cava, A. Aharony, O. Entin-Wohlman, T. Yildirim, M. Kenzelmann, C. Broholm *et al.*, Magnetically Driven Ferroelectric Order in $Ni_3V_2O_8$, Phys. Rev. Lett. **95**, 087205 (2005).

[57] Y. Yamasaki, H. Sagayama, T. Goto, M. Matsuura, K. Hirota, T. Arima, and Y. Tokura, Electric Control of Spin Helicity in a Magnetic Ferroelectric, Phys. Rev. Lett. **98**, 147204 (2007).

[58] T. Kimura, Y. Sekio, H. Nakamura, T. Siegrist, and A. Ramirez, Cupric oxide as an induced-multiferroic with high-Tc, Nat. Mater. **7**, 291 (2008).

[59] N. Hur, S. Park, P. Sharma, J. Ahn, S. Guha, and S. Cheong, Electric polarization reversal and memory in a multiferroic material induced by magnetic fields, Nature (London) **429**, 392 (2004).

[60] H. Murakawa, Y. Onose, S. Miyahara, N. Furukawa, and Y. Tokura, Ferroelectricity Induced by Spin-Dependent Metal-Ligand Hybridization in $Ba_2CoGe_2O_7$, Phys. Rev. Lett. **105**, 137202 (2010).

[61] Y. Choi, H. Yi, S. Lee, Q. Huang, V. Kiryukhin, and S.-W. Cheong, Ferroelectricity in an Ising Chain Magnet, Phys. Rev. Lett. **100**, 047601 (2008).

[62] H. Katsura, N. Nagaosa, and A. V. Balatsky, Spin Current and Magnetoelectric Effect in Noncollinear Magnets, Phys. Rev. Lett. **95**, 057205 (2005).

[63] A. Popov, D. Plokhov, and A. Zvezdin, Quantum theory of magnetoelectricity in rare-earth multiferroics: Nd, Sm, and Eu ferroborates, Phys. Rev. B **87**, 024413 (2013).